Results in Engineering 29 (2026) 109903

Contents lists available at ScienceDirect

Results in Engineering

journal homepage: www.sciencedirect.com/journal/results-in-engineering

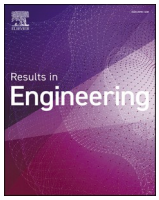

Research paper

Design and development of a novel magnetic generator of hydrodynamic cavitation

Jurij Gostiša [a,*], Matevž Dular [a], Andraž Rihar [b], Brane Širok [a], Danjel Vončina [b], Mojca Zupanc [a], Henrik Lavrič [b,*]

[a] Faculty of Mechanical Engineering, University of Ljubljana, Aškerčeva cesta 6, Ljubljana, Slovenia
[b] Faculty of Electrical Engineering, University of Ljubljana, Tržaška cesta 25, Ljubljana, Slovenia

ARTICLE INFO

Keywords:
Hydrodynamic cavitation
Rectilinear oscillator
Electromagnetic drive
Power electronics circuitry
Shock waves

ABSTRACT

This article investigates the development and evaluation of a prototype hydrodynamic cavitation generator, driven by the electromagnetically induced linear motion of a hollow piston. This so-called magnetic generator of hydrodynamic cavitation (MGHC) is designed for applications requiring small liquid volumes, with its simplicity being a key advantage. It does not require additional pumps or seals and provides a high level of sample protection against contamination. The electromagnetic drive is designed to generate a strong magnetic field, allowing for rapid acceleration of the piston and periodic generation of pressure pulsations associated with the collapse of cavitation clouds throughout the control volume of the device.

In the study, the electrical parameters of the electromagnetic drive, such as voltage, current, and frequency, were adjusted to modify the piston's motion characteristics, thereby influencing the intensity of cavitation, as reflected in the generation of intense pressure oscillations. Simultaneous pressure measurements and visualisation of cavitation structures show that the piston motion induces intense hydrodynamic cavitation along its entire stroke path, particularly during the collapse phases of cavitation clouds. The results offer qualitative and quantitative analysis of the measured variable interdependence and provide a foundation for parametric studies across different spatial and temporal scales aimed at optimising the device in the future.

1. Introduction

Cavitation is the phenomenon of sudden vaporization in liquid due to local pressure drop below the vapor pressure, followed by the collapse and condensation of the cavitation bubbles when the pressure is recuperated [1]. When cavitation bubbles and bubble clouds implode, significant amount of energy is released in the form of high pressure and heat, causing mechanical, chemical, thermal and even optical effects [2–4]. Primarily, cavitation was considered an undesirable phenomenon occurring in hydrodynamic machinery such as water turbines, pumps, propellers, etc., as it causes erosion damage to blades and other critical machine parts [5,6]. Extensive research has therefore been devoted to understanding the physical mechanisms of cavitation and its effects, and recent multi-scale investigations [7] indicate the inherently unstable nature of cavitating flows, where the interaction between macroscopic shedding and microscopic bubble dynamics results in high transient pressure loads. However, in recent years, cavitation has been recognized as having the potential to improve several liquid processing applications [8]. It is being investigated in various research areas as a process intensification method, such as organic chemical synthesis [9], in (waste)water treatment to degrade organic micropollutants, microbial disinfection or disintegration of waste sludge [10–12] and catalysis [13].

There are two most studied mechanisms of cavitation generation: acoustic cavitation (AC) and hydrodynamic cavitation (HC). In the first (Fig. 1A), the pressure and velocity conditions required for cavitation to occur can be achieved in stationary liquid using immersed oscillating objects, while in the latter (Fig. 1B-H) they occur in a flowing liquid with sufficiently strong flow dynamics. AC is generated by the ultrasonic transducer immersed in a liquid and oscillating at high frequency. When the transducer moves away rapidly, a pressure drop occurs, causing cavitation in the liquid. In contrast, HC is induced by the pressure dynamics in a fluid flow through specially designed fluidic devices that create one or more low pressure zones [14,15]. These devices, known as

* Corresponding authors.
E-mail addresses: jurij.gostisa@fs.uni-lj.si (J. Gostiša), henrik.lavric@fe.uni-lj.si (H. Lavrič).

https://doi.org/10.1016/j.rineng.2026.109903
Received 6 January 2026; Received in revised form 24 February 2026; Accepted 3 March 2026
Available online 5 March 2026

HC generators, can be broadly divided into static (without moving parts) and dynamic (with moving parts) devices. The former includes Venturi channels (Fig. 1B), orifices (Fig. 1C) and nozzles (Fig. 1D). They generate cavitation through a throttling effect, where changes in the channel cross-section cause the fluid to accelerate and decelerate, resulting in pressure drops and fluctuations. Although the cavitation generator itself has a simple geometry with no moving parts, it requires high pressure and sufficient flowrate to operate, resulting in high operating costs. Compared to static HC devices, dynamic devices use significantly different hydrodynamic principles. These devices include rotating HC generators (Fig. 1E-H) and typically exploit the pressure dynamics caused by a rotating disk with protrusions or cavities, which in combination with static elements allows for a much more energy efficient generation of low-pressure zones where cavitation occurs. The rotating disk also usually generates a sufficient pressure head so that no separate pump is required in the system, which reduces the overall construction costs and simplifies the operation of the cavitation-generating device. A few novel designs have been investigated in recent years, such as serrated discs (Fig. 1E-F) [16–18], pinned discs (Fig. 1G) [20,21] and dimpled rotors (Fig. 1H) [22]. The selection of the cavitation device design and its working principle depends on the required system size and application area. AC and static HC devices are typically used in systems with low to medium fluid flow, where simplicity and robustness of the cavitation device are more critical than energy efficiency [11]. Only AC devices are suitable for very small and isolated quantities of liquids. On the other hand, large-flow applications (e.g., wastewater and sludge treatment, disinfection) require significantly higher efficiency to be feasible, which can be achieved with rotating HC generators [20–24].

Despite the variety of HC generator designs, none are optimal for processing small liquid volumes in a highly controlled manner. Static devices, such as Venturi channels, orifices, and nozzles, require additional components like pumps, valves, and auxiliary flow channels which can contaminate the samples and affect the interpretation of the results. On the other hand, scaling down the rotating HC generators faces fundamental physical constraints. The design of the rotating shaft, the sealing mechanisms, and the required clearance tolerances impose strict geometric limitations, making miniaturization difficult. These limitations highlight the need for novel cavitation generator designs that minimize contamination risk, operate efficiently at small scales, and provide uniform, controlled cavitation without relying on complex mechanical components [25,26]. For this reason, our concept employs a non-contact electromagnetic force to drive the piston, which is a single, freely moving component without mechanical connections or seals on the wetted chamber walls. To achieve linear periodic piston motion within a limited cylinder volume, a solution based on a tubular linear machine with permanent magnets was investigated [27,28]. In such machines, currents in the stator windings create a travelling magnetic field that generates a thrust force on the magnetic piston, enabling it to move in the longitudinal direction of the stator cylinder bore. The tubular machine is just one design of linear motor that can be used to meet the requirements for linear motion in industry and transport [29].

To overcome the limitations of existing HC generators, we developed the Magnetic Generator of Hydrodynamic Cavitation (MGHC), a novel device that uses a freely moving hollow permanent magnet piston, driven by an external electromagnetic drive, to generate periodic pressure pulsations and controlled cavitation in small liquid volumes. This approach avoids the need for external pumps and seals, minimizes contamination risks, and enables precise control of cavitation dynamics. The MGHC concept, featuring a cylindrical chamber (Fig. 2– 2) housing a permanent magnet piston (Fig. 2– 1) and the external electromagnetic drive (Fig. 2– 3) is shown in the figure below.

The hydrodynamic mechanism of cavitation generation is based on the piston forcing the liquid through its coaxial orifice, which accelerates the flow and lowers the local pressure in the bore. When the pressure drops below the vapor pressure, cavitation bubbles form in the chamber. As the piston approaches the end wall, its rapid deceleration creates a pressure surge that collapses the cavitation clouds and generates shock waves that propagate throughout the chamber.

This study focuses on the development of a prototype MGHC and the experimental evaluation of its performance characteristics. Section 2 describes the design and development of the prototype as well as the experimental setup and measurement methods. Section 3 presents the results of the prototype evaluation and in-situ operational characterization, followed by a discussion of the observed cavitation dynamics and shock wave behavior. Finally, Section 4 summarizes the key findings and outlines directions for future work.

2. Methods

The primary objective of this study is to develop a novel magnetically driven generator of HC that allows precise control of cavitation dynamics in a highly controlled environment. The following section presents the methodology used to develop and evaluate the MGHC prototype. First, the technical aspects of the device design and

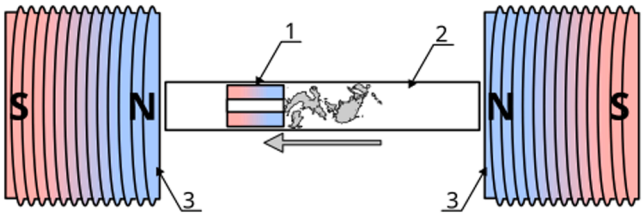

Fig. 2. Schematical representation of Magnetic Generator of Hydrodynamic Cavitation (MGHC), featuring 1 – permanent magnet piston with through channel – hollow piston, 2 – cavitation chamber, 3 – electromagnetic drive.

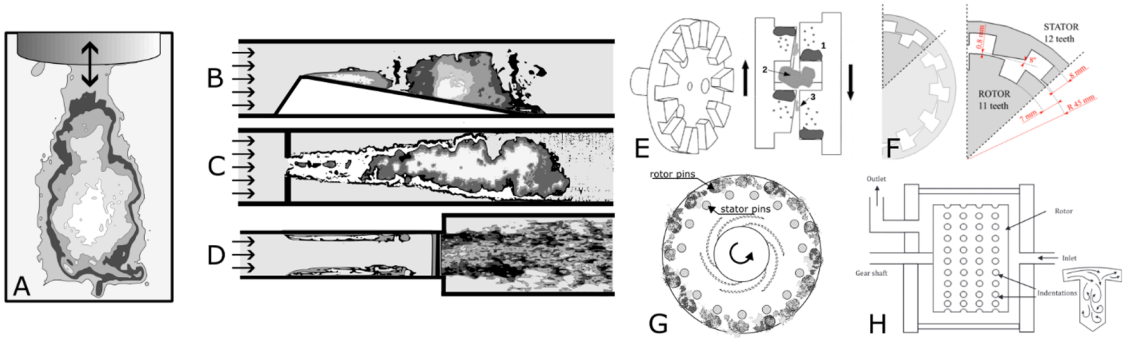

Fig. 1. Cavitation generation concepts and corresponding devices: **A)** Ultrasonic transducer, **B)** Venturi channel, **C)** orifice, **D)** nozzle, **E)** rotational generator of HC with a serrated disk and axial gap [16], **F)** rotational generator of HC with a serrated disk and radial gap [19], **G)** rotational generator with a disk and pins [20], and **H)** drum generator with cavities [22]. Cavitation generation mechanisms A-D were drawn by the author.

construction are described, comprising the electromagnetic drive with control electronics and cavitation module. Next, the experimental setup and measurement procedures are outlined, followed by a description of the prototype evaluation and in-situ operation characterization used to analyze piston motion, pressure dynamics, and cavitation behavior.

2.1. Electromagnetic drive and cavitation module development

The MGHC consists of two main systems, the electromagnetic drive and the cavitation module. The electromagnetic drive converts the electrical energy into the magnetic energy required to accelerate the hollow piston along the entire stroke of the cavitation chamber. The electromagnetic drive of the MGHC consists of three main parts: the ferromagnetic core, the electromagnetic coils, and the drive electronics (Fig. 3-left and Fig. 4- 1, 2).

The drive electronics converts the DC supply voltage into the required voltage pulses (Fig. 3-right). It is based on an electronic circuit, which comprises a standard H-bridge inverter with four SEMIKRON SKM453A020 MOSFET modules ($V_{nom} = 200$ V, $I_{max} = 450$ A), transient voltage suppression diodes (LITTELFUSE 5KP120CA), and a DC-link capacitor bank ($C_{DC} = 35$ mF) for energy storage. The MOSFET modules are driven by SKHI22A drivers, while the inverter is controlled by a C2000 Delfino microcontroller (LaunchXL-F28379D) from Texas Instruments. The microcontroller generates drive signals for activation of diagonal MOSFET pairs (M1-M4, M2-M3) to generate pulses of bipolar output voltage with two voltage levels ($\pm V_{DC}$). The microcontroller enables open-loop control with settings for pulse number, duration, and frequency. Longer time voltage pulses are produced when MOSFET pairs are activated, while short time pulses are induced when core magnetic energy needs to be released after deactivating the MOSFETs. Each long-short pulse cycle concludes with dead time, namely a pause with all MOSFETs turned off, before activating the opposite MOSFET pair. This pause is required to prevent short circuit of transistor legs. In this way, positive and negative current pulses are generated. The theoretical shapes of the voltage and associated current pulses are shown in (Fig. 3-right).

The ferromagnetic core is made from E-shaped laminated sheet metal for transformers (M530–50A, magnetic saturation 1.4 T) and is designed to form a good conductive path for magnetic field. The inner limbs of the cores are shortened to accommodate the cavitation module (Fig. 4– 3). The cut-off sections of the main limbs are attached to the side limbs, functioning as magnetic field concentrators. These concentrators improve the distribution of the magnetic field and increase the force on the magnet by up to 35 %. The core is mechanically reinforced with FR4 sheets to secure the device and minimize vibrations. Two electromagnetic coils, each wound with 100 turns of Litz wire with a cross-section of 6 mm^2 (inductance: 3.21 mH, resistance: 91 mΩ) are mounted one on each main limb of the ferromagnetic core. They are connected in series and are fed by the bipolar voltage pulses of the drive electronics in a way to generate opposing electromagnetic fields. Combined with the field of the permanent magnet piston, this configuration produces alternating attractive and repulsive forces (Fig. 2), transforming the electromagnetic energy into kinetic energy of the rectilinearly moving piston inside the cavitation chamber.

The cavitation module (Fig. 4– A) is made of acrylic glass and consists of a cavitation chamber housing and two cover plates on the top and bottom of the housing. The housing features a 60 mm long cylindrical cavitation chamber with a diameter of 10.2 mm (Fig. 4– B). The piston (Fig. 3– C) has a cylindrical shape with a diameter of 10 mm and a length of 10 mm as well as a cylindrical bore (channel) with a diameter of 4 mm in the center axis of the piston. The piston is made of sintered rare earth neodymium (nickel plated, N42 strength). The cover plates of the cavitation module have inlet and outlet channels through which the sample liquid is introduced and pressed out. The tube fittings, with which the inlet and outlet tubes are attached, are located at the outermost point of the cap walls. A valve is fitted in front of the inlet and behind the outlet fitting to seal the cavitation chamber during operation.

2.2. Prototype evaluation

The MGHC prototype was evaluated step by step to assess electromagnetic drive performance, magnetic force generation, and cavitation behavior. First, the electromagnetic drive was characterized through electrical measurements to verify component selection and control strategy. Mechanical performance was assessed in terms of noise, vibration, and harshness (NVH). Magnetic force was then measured using a dynamometer to quantify operational characteristics. Secondly, the prototype was tested in-situ to evaluate cavitation dynamics and understand the generation mechanisms. Finally, as the shock waves were observed, a propagation analysis was performed, using a method described by Petkovsek [30].

2.2.1. Electromagnetic drive design evaluation

Oscilloscope-based measurements of key electric quantities of the electromagnetic drive were performed to estimate appropriateness of the design. Parameters of the drive circuitry, such as the power supply voltage, dead-time, and the trigger pulse duration were changed to evaluate their effects on operation of the electromagnetic drive and to test its suitability. The power electronics circuitry (the H-bridge inverter) was supplied by an ITECH IT6010C-80–240 bidirectional power supply, which allows for the DC link voltage to be set to arbitrary values. The upper limit value was defined by the power MOSFETs breakdown voltage or by the maximum current through the coils. A Tektronix DPO4034B 350 MHz oscilloscope was used in conjunction with TESTEC 25 MHz differential voltage probes and a dedicated current probe ILA800 for voltage and current measurements. Obtained waveforms (pulse-width-modulated MOSFET driver voltage signal, DC-link voltage, output voltage and coil current) were transferred to MATLAB for further data processing, such as estimation of supply voltage ripple, evaluation of maximum current values, and other metrics.

During the experiments, overheating of the electromagnetic drive was observed due to repeated high-current pulses, primarily caused by resistive losses in the coils. Without additional cooling, the coil temperature increased to a level that could damage the insulation and

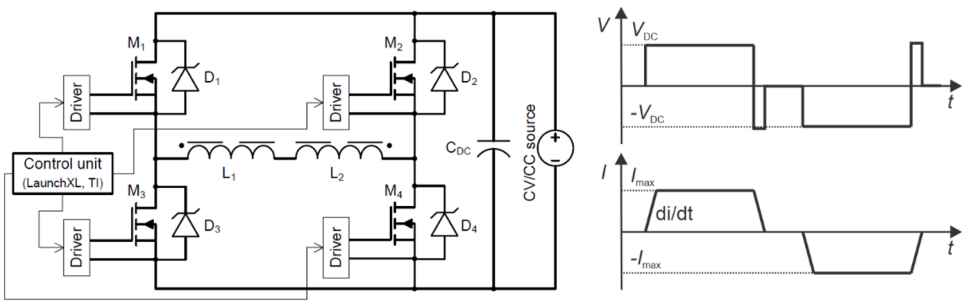

Fig. 3. Simplified electrical diagram of electromagnetic drive (left) and theoretical voltage and current waveforms (right).

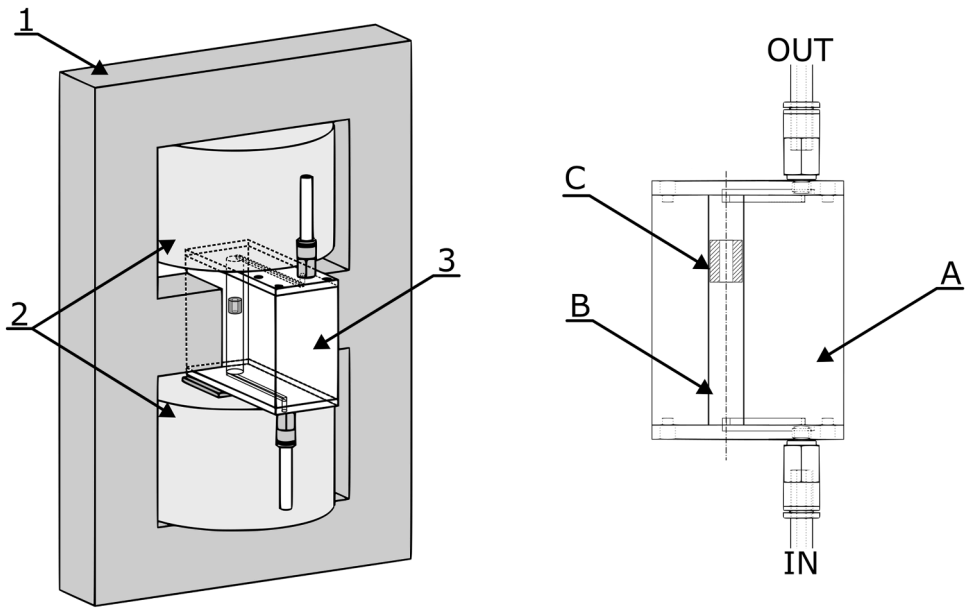

Fig. 4. Schematical representation of the MGHC prototype with key elements (left) and the cavitation module (right). 1 – ferromagnetic core, 2 – electromagnetic coils, 3 – cavitation module, A – acrylic housing, B – cavitation chamber, C – hollow permanent magnet piston.

compromise stable operation of the drive electronics. The design was therefore upgraded by installing low-voltage fans directed at the coils and power electronics to enhance convection cooling (Fig. 5). This ensured reliable operation of the drive and did not significantly influence the liquid in the cavitation chamber. Since the experimental runs were short (several seconds), no significant temperature rise was expected and thermal effects on cavitation characteristics were considered negligible. In terms of noise, vibrations, and harshness the system turned out to be very reliable and stable, which is a consequence of the robust design and the used FR4 sheets for core reinforcement.

Furthermore, a separate static experiment was carried out to evaluate the magnetic force on the permanent magnet piston and thereby characterize the electromagnetic drive independently of the cavitation experiments. For this purpose, the prototype was equipped with a loadcell mechanism and a specially designed holder to measure the magnetic force exerted on the permanent magnet piston in the opening of the cavitation chamber under stationary conditions. Fig. 5- right schematically depicts that measurement apparatus. The load cell was positioned at the top of the device (Fig. 5- A), outside the strong magnetic field, to prevent parasitic magnetic forces. The holder structure, made of FR4 material and mounted with non-ferromagnetic screws, allowed height adjustments, allowing the position of the magnet to be varied along its stroke path in the chamber opening (Fig. 5- B). The load cell's signal was digitized and processed using the NI cDAQ-9174 system with NI-9219 module and LabView software. Before each measurement, the combined self-weight of the supporting holder structure and the magnet was determined, ensuring that the recorded results reflected the actual magnetic force. The force measurement system was validated using calibrated weights, yielding deviations of approximately 0.5 % for weights between 100 g and 1000 g and approximately 2 % for weights of 50 g and below. Magnetic force measurements were performed for coil current levels 25 A, 50 A, 100 A, and 200 A at different piston positions along the entire stroke length.

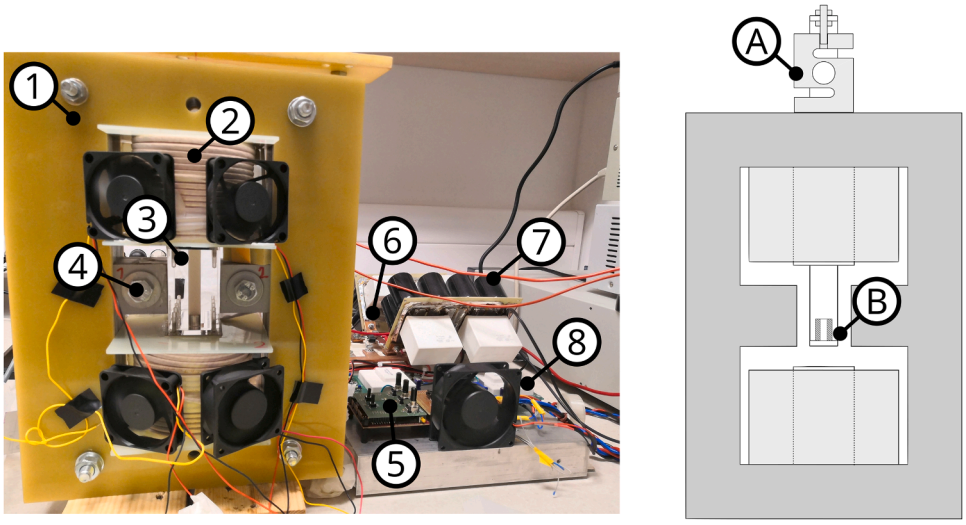

Fig. 5. MGHC prototype with the cavitation module (left). 1 – ferromagnetic core with reinforcement FR4 sheets, 2 – electromagnetic coils, 3 – cavitation module, 4 – magnetic field concentrators, 5 – microcontroller, 6 – MOSFET modules, 7 – DC link capacitor bank, 8 – MOSFET drivers. MGHC drive equipped with a dynamometer apparatus, used to measure force on the permanent magnet (right): A – load cell, B – magnet positioned on the holder structure.

2.2.2. Prototype in-situ operation characterization

After successful testing of the electromagnetic drive design, the system was equipped with the developed cavitation module and prototype in-situ operation characterization was performed. The configuration of the electromagnetic drive and the measurement equipment for evaluating key electric quantities was similar as described above (see Chapter 2.2.1).

To characterize the HC dynamics in the MGHC cavitation chamber, high-speed visualization and pressure measurements were performed. Pressure dynamics in the cavitation chamber induced by the piston movement and cavitation onset, was quantified using a Teledyne Reson TC4013 hydrophone (Fig. 6– $p(t)$), which was installed at a 90° angle to the cavitation chamber wall. The hydrophone signal was amplified with a Teledyne Reson EC6081 preamplifier and sampled with 300 kHz using National Instruments cDAQ NI-9174 and NI-9222 measurement card. The cavitation extent, bubble cloud dynamics and shock wave propagation were investigated using high-speed imaging. Photron Mini UX100 high-speed camera was placed perpendicularly to the meridian plane of the cavitation chamber, while illumination was set on the opposite side of the chamber to achieve high contrast of the cavitating flow as darker structures on a brighter background. Images with 1280 × 248 resolution were acquired at 16,000 frames per second. The piston was optically tracked to obtain the piston velocity time series (Fig. 6– $v(t)$), Grey-value was calculated in the box behind the piston (Fig. 6– $s(t)$), to quantify the cavitation cloud extent. The velocity $v(t)$ and grey-value time series $s(t)$ were synchronized to the acquired pressure signals $p(t)$ and the electric current of the electromagnetic drive $I(t)$ and used to characterize the prototype in-situ operation.

As part of the test procedure, the hollow permanent magnet piston was inserted into the cavitation chamber, chamber was closed and filled with water. The periodic excitation of the piston was performed with various settings of the electrical parameters, such as adjustments to power supply voltage levels and maximum current limits, as well as duration, number, and frequency of high current pulses. The idea behind changing the parameters within the adjustable ranges was to experimentally achieve optimal performance from an electrical point of view in order to ensure the highest levels of cavitation intensity. Electrical and hydrodynamic measurements were performed and results acquired simultaneously to determine the relationships between the shape of the waveform of the current pulses, the piston position dynamics (position, velocity, acceleration) and the cavitation extent and dynamics. During the in-situ operation experiments, the valves were closed so that the experimental system was isolated from its surroundings, maintaining a constant volume of approximately 5 mL of degassed water at a temperature of 20 °C and initial absolute pressure of 1 bar (ambient air pressure).

2.2.3. Shock wave analysis

A shock wave was identified at the point of piston impacting the end wall. A methodology introduced by Petkovsek [30] was used to determine the transition and amplitude of the shock waves that were emitted at cavitation cloud collapses. Without image postprocessing it is nearly impossible to see the passage of the shock wave. However, a close observation reveals a “darker region” moving in an oscillatory motion through the domain. When the volume is seeded with small bubbles (as in the present case) the slight change in brightness is caused by the light attenuation by the bubbles, which change in size due to the passage of the shock wave. In other words, as the shock wave passes a bubble, the bubble shrinks in size. On a macroscopic level, inside the bubbly flow, this can be seen as a slight decrease in image intensity. According to Petkovšek [30], the shock wave amplitude can then be estimated by Eq. (1):

$$p_\infty = p_v + \left(p_{\infty,0} - p_v + \frac{2\sigma}{R_0}\right)\left(\frac{R_0}{R}\right)^{3\kappa} - \frac{2\sigma}{R} \tag{1}$$

which depends only on constants vapor pressure p_v, surface tension σ and polytropic constant κ, the reference measurements of $p_{\infty,0}$ and R_0 and the current bubble radius R. The latter one needs to be determined by polynomial calibration function, which relates the R to the brightness of the image and further on to the reference pressure measurements at a single location [30].

3. Results and discussion

The following chapter presents key results of the study, focusing firstly on the electrical and physical aspects of in-situ operation characterization, where the dynamic behavior of the prototype was analyzed in connection to the evolution of cavitation topology, and secondly on the in-depth analysis of shock waves, induced by the impact of the piston on the end plate. Taken together, these investigations provide crucial insights into the coupling between the electromagnetic drive, the piston dynamics and cavitation phenomena, and enable a comprehensive understanding of the prototype's operation and performance.

3.1. Characterization of electromagnetic drive in terms of electric quantities and electromagnetic force

The two time series diagrams in Fig. 7 shows the source supply voltage waveforms, i.e., the voltages across the DC link capacitor V_{DC}, pulse-width-modulated MOSFET driver signals V_{PWM}, and the current I and voltage of the coils V_{OUT}, which were captured with an oscilloscope. The waveforms are for the case when DC link voltage was set to $V_{DC} = 50$ V, which enabled reaching maximum currents of $I = 220$ A. This is also effectively the maximum capacity permitted by the configuration.

When one diagonal of MOSFETs is turned on, the coils start to conduct the slowly increasing current, resulting in increasing force on the magnet moving across the cavitation chamber. The slew rate of coil current (first part of the waveform) is determined with the supply voltage and with the coil parameters (R_{coil}, L), while the maximum current (second part of the waveform) is determined only with the supply voltage and the coil resistance R_{coil}. Apart from the theoretical waveform, the actual coil current’s slew rate is lower, resulting in the

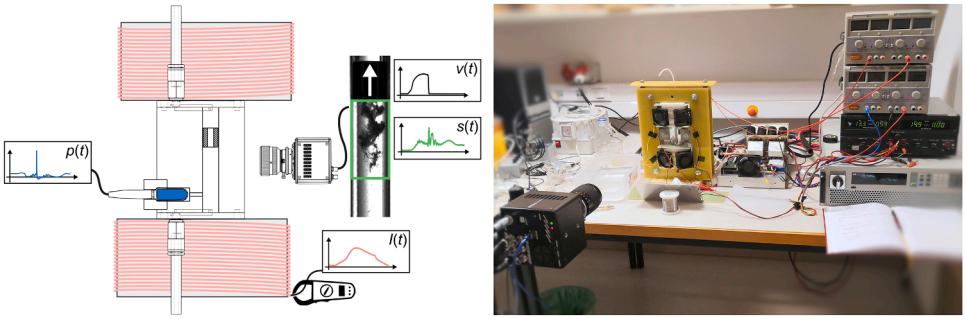

Fig. 6. Experimental setup for pressure measurement and flow imaging in the MGHC.

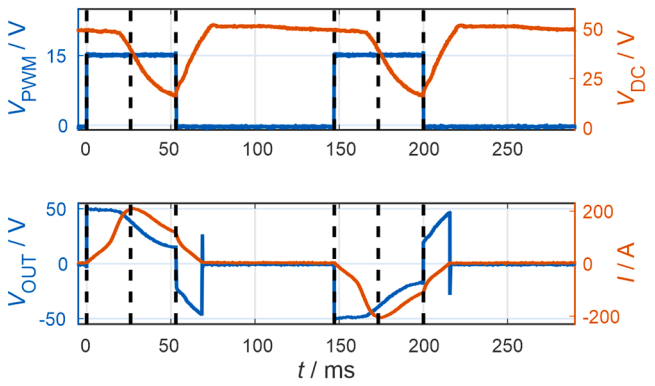

Fig. 7. Oscilloscope-based measurement results of key electric quantities for one cycle of positive and negative output voltages, plotted in MATLAB.

maximum current level and consequently the force being reached relatively late, in fact just before the magnet touches the other side of the chamber (Fig. 10).

The results evidently demonstrate that in view of electromagnetic performance the device behaves somewhat differently from the theoretically expected behaviour. Comparison of acquired oscillograms of output voltage and coil current (Fig. 7) with the theoretical voltage-current waveforms (Fig. 3. - right) shows certain limits of the real electromagnetic system, as it turns out that the actual coil current and output voltage are not trapezoidal and rectangular, respectively. Since the power of the voltage power supply is limited, as is the amount of stored electrical energy in the DC link capacitors, the DC voltage starts to gradually decrease when the coil currents are near their maximum values, resulting in a drop of available power. The non-constant DC voltage is also the main reason for the non-rectangular voltage and non-trapezoidal current waveforms.

Fig. 8 shows the results of the measured static magnetic force exerted on a permanent magnet as a function of the magnet's position inside the cavitation chamber opening for four current intensities. The polarity of the magnet and the magnetic field of the coils were such that the attractive force prevailed at positions below 30 mm, while the repulsive force prevailed at positions above 30 mm. The results of the measured forces show that increasing the power supply voltage, and consequently the coil current, leads to higher overall forces and more pronounced local extrema of the magnetic force at the piston's near-end positions (10 mm and 50 mm). This positively affects the expected increase in cavitation due to the elevated velocity gradients of the piston at the test tube's end positions and facilitates the formation of shock waves in the final phase of piston motion. The decrease in force at the extreme positions of the magnet is noteworthy. It is logical that the force at the 55 mm position is smaller than at 50 mm, as the repulsive force decreases

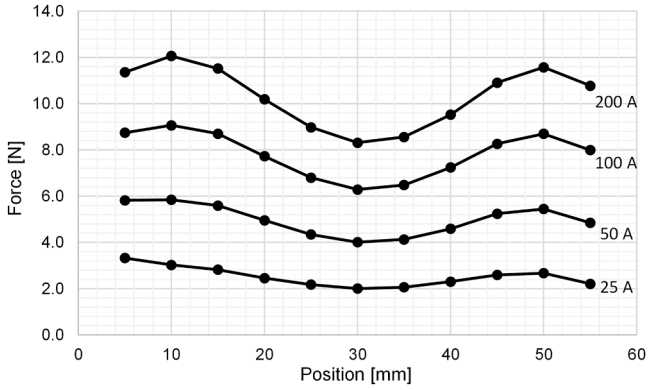

Fig. 8. Measured forces on the magnet at different current levels and magnet positions within the core opening.

due to the attractive force between the magnet and the ferromagnetic core. Similarly, the force measured at the 5 mm position of the magnet should be greater than at 10 mm, but a decrease is also observed at higher current values. This phenomenon has no significant effect on the operation of the MGHC, but we assume it results from local saturation of the ferromagnetic core due to the proximity of the permanent magnet and the consequent redistribution of the local magnetic field.

3.2. *In-situ operation characterization*

The motion of the permanent magnet piston and the corresponding cavitation dynamics were analyzed using high-speed imaging used to determine the cavitation cloud topology dynamics and piston velocity, and synchronized to measurements of electric current and hydrophone pressure fluctuation time series. Fig. 9 illustrates the typical piston stroke, while Fig. 10 depicts the accompanying temporal evolution of the measured properties accompanying the cavitation induced phenomena.

Fig. 9 depicts the complete stroke of the hollow piston from one end of the cavitation chamber to the other. As the piston moves, a jet is ejected at high velocity from the back of the piston due to the bore in the piston, which is 6.25 times smaller in cross-section than the piston and the cylindrical chamber. This geometric feature causes the liquid to accelerate through the bore at a velocity approximately 6.25 times greater than the velocity of the piston. The high jet velocity leads to cavitation of the liquid in the chamber when it reaches about 19 m/s, i.e. when the piston is moving at approximately 3 m/s. The resulting cavitation cloud consists of complex shaped vapor structures exiting the piston bore. Such cavitation cloud trail becomes visible at these velocity thresholds and persists throughout the stroke until the piston impacts the flat end plate of the chamber. For comparison with conventional hydrodynamic cavitation systems, the cavitation number $\sigma = \frac{p_\infty - p_v}{\frac{1}{2}\rho U^2}$, where p_∞ is the ambient pressure, vapor pressure p_v can be approximated using the jet velocity as the characteristic velocity U. Using ambient pressure and water properties at room temperature, piston velocities of 3–4.5 m/s (corresponding to jet velocities of approximately 19–28 m/s) yield $\sigma \approx 0.6$–0.25, which agrees with the developed cavitation regime observed in the experiments. At piston velocities around 3 m/s the estimated cavitation number approaches $\sigma \approx 0.6$, which coincides with the experimentally observed cavitation onset and is considered within the typical cavitation inception range. Due to the transient and spatially non-uniform pressure field in the MGHC, this value should be regarded as an order-of-magnitude estimate.

The kinematics of the piston stroke was analyzed using an algorithm that determines the piston position and velocity $v(t)$ (black curve in Fig. 10). The stroke motion can be divided into three phases: an initial acceleration phase lasting 10 ms, a plateau phase at around $t = 10$ ms lasting 15 ms and instant deceleration due to the impact at $t = 25$ ms. The time series of the piston velocity (black curve on Fig. 10) and the shift with respect to the current time series (red curve Fig. 10) suggest that a steeper current curve could increase the acceleration slope, while a reduction of the current immediately after the piston impact could reduce the overall energy consumption.

To quantify the cavitation cloud dynamics, the greyscale variable $s(t)$ was introduced. It represents the vapor phase fraction in the region of interest at the trailing edge of the piston. This metric allows the evaluation of the dynamics of the cavitation cloud size and its correlation to other measured variables. As can be seen, based on the pressure time series in the Fig. 10 and visually observed in the Fig. 9, cavitation onset occurs at $t = 12.5$ ms, followed by a gradual expansion until $t = 15$ ms. Once the cavitation cloud is fully developed, its size remains relatively stable until the impact at $t = 25$ ms. During this phase, the topology of the cavitation cloud follows the jet dynamics, which is characterized by short pulsations and a swirling pattern. It is noteworthy that the pressure fluctuation curve coincides with the grey-level curve, which is expressed

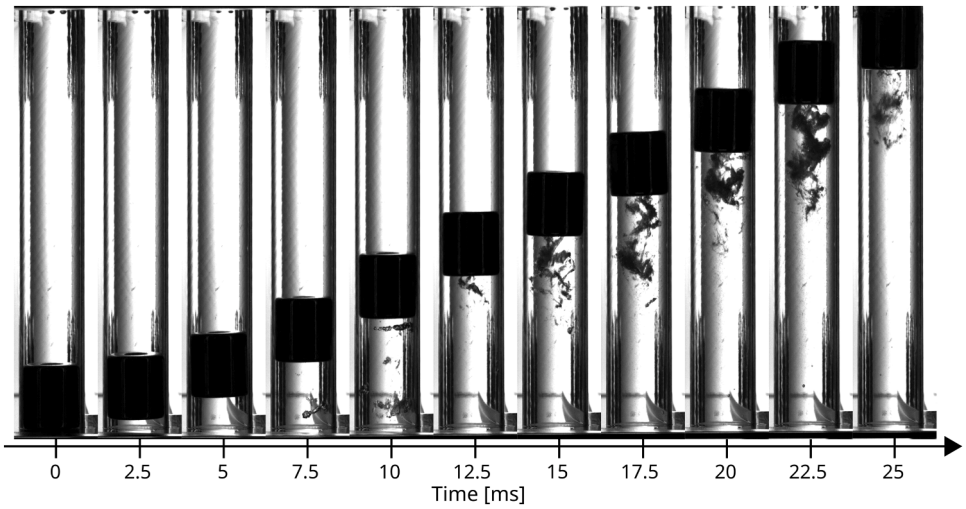

Fig. 9. High-speed image sequence of the typical piston stroke in the cavitation chamber.

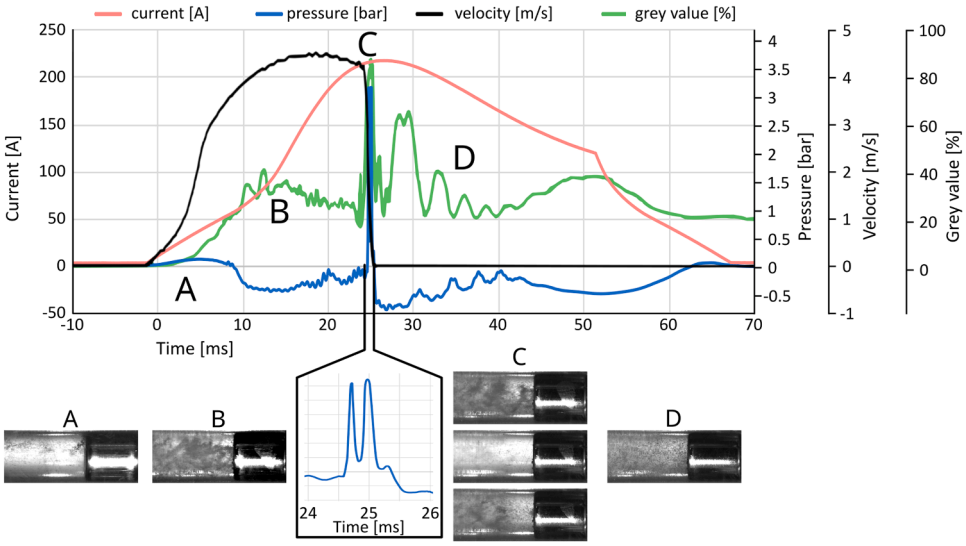

Fig. 10. Current $I(t)$, pressure $p(t)$, velocity $v(t)$ and grey value $s(t)$ time series is graphed as a function of time for a typical piston stroke. Below the graph, typical cavitation cloud topology is shown for each distinct stroke phase. Image sequence A-D depicts the typical stroke phases: A – initial idle state, B – cavitation onset, C – piston impact with the end wall, D – late vapor phase fluctuation.

by a negative pressure deviation with increasing greyscale value.

In the early phase of the stroke (Fig. 10– B), multiphase flow can be observed as cavitation clouds emerge from the piston bore and mix with the surrounding liquid. However, upon abrupt deceleration at $t = 25$ ms, the cavitation structures rapidly collapse due to a sudden pressure surge. This can be seen in Fig. 10– C, where the liquid appears much clearer and brighter. At this time point, a sharp pressure peak is detected, corresponding to the almost instantaneous collapse of all cavitation bubbles in the entire chamber within a single 62.5 μs image. The data confirms that 2–3 consecutive local pressure peaks occur within the impact window of 3.5 ms, accompanied by a rapid fluctuation in vapor fraction directly visible in the evolution of the cavitation topology. This phenomenon is attributed to the induced shock wave, propagating from the impact point towards the opposite end of the cavitation chamber and is further investigated in the following chapter. At later times (Fig. 10– D), a low frequency vapor phase fluctuation occurs accompanied by in-phase low frequency and amplitude pressure fluctuations. The latter is attributed to the cavitation module dynamic response and its natural frequency.

3.3. Shock wave dynamics characterization

A critical transition in the cavitation topology occurs when the piston impacts the end plate of the cavitation chamber. The high-speed images in Fig. 11 show this transition within the 3.5 ms deceleration window. Although pressure fluctuation $p(t)$ measurements provide some insight into the pressure dynamics in the cavitation chamber, these were only taken at a single location and do not reveal the local pressure conditions across the entire volume of liquid. Since the flow field was seeded by bubbles, during most of the piston passage from one end of the cavitation chamber to the other, we were able to use the size and grey level value of bubbles for optical estimation of the pressure amplitude. This way pressure estimation on the sequence of images recorded immediately after the piston collision (denoted as $t = 0$ ms on Fig. 11) with the bottom end plate, was performed.

At $t = 0.25$ ms, the maximum pressure amplitude of approximately 10 bars was calculated. The movement of the high-pressure zone away from the impacting piston indicates formation of a shock wave, likely due to the combined effect of water hammer upon the abrupt stopping of the piston, as well as cavitation structure collapse triggered by a sudden

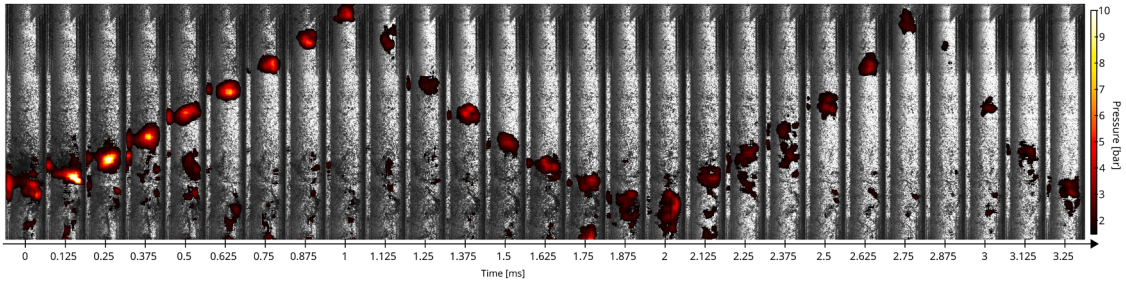

Fig. 11. Calculated pressure magnitude in the zone of collapsing cavitation structures after the impact of the hollow magnetic piston with the bottom end plate. The position of the main high-pressure zone is consistent with shock wave propagation.

surge in liquid pressure. The shock wave can be seen propagating towards the upper end plate of the chamber where it is reflected towards the piston while its pressure amplitude gradually diminishes. The initial shock wave propagation velocity can be estimated to be 56 m/s. This relatively slow shock wave velocity is a result of the presence of the gaseous phase (bubbles) in liquid, which is highly compressible and well known to reduce the effective speed of sound [2,31]. This can be further confirmed by the increase of the shock propagation velocity during the second (72 m/s), third (84 m/s) and fourth (126 m/s) passage as the number of bubbles gradually reduces and the mixture becomes less compressible.

4. Conclusions

The described proof-of-concept study was performed with the main goal of assessing the feasibility of generating hydrodynamic cavitation by the electromagnetically driven piston. Obtained results confirm the suitability of the designed prototype, demonstrating the ability of achieving sufficient acceleration and piston velocities to achieve cavitation. Nevertheless, the presented study naturally has some shortcomings. Firstly, the prototype was only tested with water sample and secondly, a limited amount of electromagnetic drive parameters were tested in with respect to operation optimization. Hence, the energy amount required to achieve cavitation is relatively high compared to established approaches of cavitation generation.

To address these drawbacks, future work will be focused on several different aspects. Expected are: i) further testing of resulting cavitation effects, performing tests also on liquids with bacteria and other materials interesting for the chemical and pharmaceutical industries, ii) further device optimization, especially in terms of reducing required electromagnetic energy and increasing the force on the magnet, and iii) testing of new power electronics control algorithms, again in relation to performance optimization. More specifically, slew rate of the current could be increased by increasing the supply voltage. Increased slew rate would result in increased intervals of high forces and presumably in higher magnet acceleration, linked to stronger cavitation effects. However, such modification would lead to required adjustments of coil parameters to avoid exceeding normative MOSFET current levels. Secondly, the set duty cycles of MOSFET control signals could be adjusted to match the magnet's time-of-flight and avoid unnecessary power losses when the magnet is already on the other side of the cavitation chamber. This would result in efficiency optimization, improved cooling of coils, and most importantly in lower DC voltage ripple with more rectangular-like voltage waveforms.

Introduction of a coupled multiphysics numerical simulation analyses of electromagnetic, thermal, mechanical, and fluid dynamics phenomena is expected to enable further optimization of the cavitation chamber and electromagnetic drive design. The device proved to be an effective method for generating HC and pressure waves for small liquid volumes without requiring auxiliary pumps or complex sealing, while also eliminating the risk of fluid contamination and cavitation-induced erosion of the device. Obtained results confirm the strong potential of the presented principle, verifying the sensibility of further work on the subject at hand and presenting a platform for further research in this field.

CRediT authorship contribution statement

Jurij Gostiša: Writing – original draft, Methodology, Investigation, Data curation, Conceptualization. **Matevž Dular:** Writing – review & editing, Supervision, Project administration, Funding acquisition. **Andraž Rihar:** Writing – review & editing, Writing – original draft, Methodology, Investigation, Data curation, Conceptualization. **Brane Širok:** Writing – review & editing, Writing – original draft, Visualization, Methodology, Investigation, Conceptualization. **Danjel Vončina:** Writing – review & editing, Supervision, Project administration, Funding acquisition. **Mojca Zupanc:** Writing – review & editing, Writing – original draft, Resources, Formal analysis, Data curation. **Henrik Lavrič:** Writing – review & editing, Writing – original draft, Methodology, Investigation, Formal analysis, Data curation, Conceptualization.

Declaration of competing interest

The authors declare no competing financial interest.

Acknowledgements

This work was supported by the Slovenian Research Agency (Research Core Funding No P2-0401, P2-0422, P2-0258, and Research Projects No N2-0381, N2-0376, J2-4480, J2-60032).

Data availability

Data will be made available on request.

References

[1] J.-P. Franc, J.-M. Michel, *Fundamentals of Cavitation*. in Fluid Mechanics and its Applications, Springer Netherlands, Dordrecht, 2005, https://doi.org/10.1007/1-4020-2233-6.
[2] C.E. Brennen, C.E. Brennen, *Cavitation and Bubble Dynamics*. in Oxford Engineering Science Series, Oxford University Press, Oxford, New York, 1995.
[3] K.S. Suslick, N.C. Eddingsaas, D.J. Flannigan, S.D. Hopkins, H. Xu, Extreme conditions during multibubble cavitation: sonoluminescence as a spectroscopic probe, Ultrason. Sonochem. 18 (4) (2011) 842–846, https://doi.org/10.1016/j.ultsonch.2010.12.012. Jul.
[4] S. Koda, T. Kimura, T. Kondo, H. Mitome, A standard method to calibrate sonochemical efficiency of an individual reaction system, Ultrason. Sonochem. 10 (3) (2003) 149–156, https://doi.org/10.1016/S1350-4177(03)00084-1. May.
[5] M. Binama, A. Muhirwa, and E. Bisengimana, 'Cavitation effects in centrifugal pumps- A review', vol. 6, no. 5, 2016.
[6] Y. Cui, F. Guo, Q. Ding, B. Cheng, Investigation of cavitation damage patterns in centrifugal pump blades under rotating flow fields, J. Pipeline Sci. Eng. (2025) 100288, https://doi.org/10.1016/j.jpse.2025.100288. Apr.
[7] Z. Wang, H. Cheng, B. Ji, X. Peng, Numerical investigation of inner structure and its formation mechanism of cloud cavitating flow, Int. J. Multiph. Flow 165 (2023) 104484, https://doi.org/10.1016/j.ijmultiphaseflow.2023.104484. Aug.

[8] M.G. Galloni, V. Fabbrizio, R. Giannantonio, E. Falletta, C.L. Bianchi, Applications and applicability of the cavitation technology, Curr. Opin. Chem. Eng. 48 (2025) 101129, https://doi.org/10.1016/j.coche.2025.101129. Jun.
[9] R.F. Martínez, G. Cravotto, P. Cintas, Organic sonochemistry: a chemist's timely perspective on mechanisms and reactivity, J. Org. Chem. 86 (20) (2021) 13833–13856, https://doi.org/10.1021/acs.joc.1c00805. Oct.
[10] M. Dular, Hydrodynamic cavitation damage in water at elevated temperatures, Wear 346–347 (2016) 78–86, https://doi.org/10.1016/j.wear.2015.11.007. Jan.
[11] M. Gągol, A. Przyjazny, G. Boczkaj, Wastewater treatment by means of advanced oxidation processes based on cavitation – a review, Chem. Eng. J. 338 (2018) 599–627, https://doi.org/10.1016/j.cej.2018.01.049. Apr.
[12] M. Zupanc, et al., The use of hydrodynamic cavitation for waste-to-energy approach to enhance methane production from waste activated sludge, J. Environ. Manag. 347 (2023) 119074, https://doi.org/10.1016/j.jenvman.2023.119074. Dec.
[13] M.H. Abdurahman, A.Z. Abdullah, N.F. Shoparwe, A comprehensive review on sonocatalytic, photocatalytic, and sonophotocatalytic processes for the degradation of antibiotics in water: synergistic mechanism and degradation pathway, Chem. Eng. J. 413 (2021) 127412, https://doi.org/10.1016/j.cej.2020.127412. Jun.
[14] G. Mancuso, M. Langone, G. Andreottola, A critical review of the current technologies in wastewater treatment plants by using hydrodynamic cavitation process: principles and applications, J. Environ. Health Sci. Eng. 18 (1) (2020) 311–333, https://doi.org/10.1007/s40201-020-00444-5. Jan.
[15] X. Sun, et al., A review on hydrodynamic cavitation disinfection: the current state of knowledge, Sci. Total Environ. 737 (2020) 139606, https://doi.org/10.1016/j.scitotenv.2020.139606. Oct.
[16] M. Petkovšek, M. Mlakar, M. Levstek, M. Stražar, B. Širok, M. Dular, A novel rotation generator of hydrodynamic cavitation for waste-activated sludge disintegration, Ultrason. Sonochem. 26 (2015) 408–414, https://doi.org/10.1016/j.ultsonch.2015.01.006. Sep.
[17] J. Vilarroig, R. Martínez, E. Zuriaga-Agustí, S. Torró, M. Galián, S. Chiva, Design and optimization of a semi-industrial cavitation device for a pretreatment of an anaerobic digestion treatment of excess sludge and pig slurry, Water Environ. Res. 92 (12) (2020) 2060–2071, https://doi.org/10.1002/wer.1366. Dec.
[18] L. Xue, et al., Investigation on the cavitation characteristic of a novel cylindrical rotational hydrodynamic cavitation reactor, Ultrason. Sonochem. 109 (2024) 106999, https://doi.org/10.1016/j.ultsonch.2024.106999. Oct.
[19] J. Vilarroig, R. Martínez, E. Zuriaga-Agustí, S. Torró, M. Galián, S. Chiva, Design and optimization of a semi-industrial cavitation device for a pretreatment of an anaerobic digestion treatment of excess sludge and pig slurry, Water Environ. Res. 92 (12) (2020) 2060–2071, https://doi.org/10.1002/wer.1366.
[20] J. Gostiša, M. Zupanc, M. Dular, B. Širok, M. Levstek, B. Bizjan, Investigation into cavitational intensity and COD reduction performance of the pinned disc reactor with various rotor-stator arrangements, Ultrason. Sonochem. 77 (2021) 105669, https://doi.org/10.1016/j.ultsonch.2021.105669. Sep.
[21] J. Gostiša, et al., Performance evaluation of a novel pilot-scale pinned disc rotating generator of hydrodynamic cavitation, Ultrason. Sonochem. 72 (2021) 105431, https://doi.org/10.1016/j.ultsonch.2020.105431. Apr.
[22] B. Maršálek, Š. Zezulka, E. Maršálková, F. Pochylý, P. Rudolf, Synergistic effects of trace concentrations of hydrogen peroxide used in a novel hydrodynamic cavitation device allows for selective removal of cyanobacteria, Chem. Eng. J. 382 (2020) 122383, https://doi.org/10.1016/j.cej.2019.122383. Feb.
[23] B. Wang, H. Su, B. Zhang, Hydrodynamic cavitation as a promising route for wastewater treatment – a review, Chem. Eng. J. 412 (2021) 128685, https://doi.org/10.1016/j.cej.2021.128685. May.
[24] C. Agarkoti, P.D. Thanekar, P.R. Gogate, Cavitation based treatment of industrial wastewater: a critical review focusing on mechanisms, design aspects, operating conditions and application to real effluents, J. Environ. Manage. 300 (2021) 113786, https://doi.org/10.1016/j.jenvman.2021.113786. Dec.
[25] A. Hordieiev, G. Kalda, M. Pashechko, A. Hanzyuk, V. Tkachuk, N. Kostiuk, Study of the influence of cavitation and magnetic field on the change of water properties and its purification in a vibrating machine with determination of drive modes, Adv. Sci. Technol. Res. J. 18 (3) (2024) 234–245, https://doi.org/10.12913/22998624/186545. Jun.
[26] I. Aftanaziv, V. Korendiy, O. Kachur, O. Strogan, I. Svidrak, R. Stotsko, Design peculiarities and mathematical model of an enhanced low-frequency vibratory cavitation device, Vibroeng. Procedia 51 (2023) 1–7, https://doi.org/10.21595/vp.2023.23577. Oct.
[27] J. Wang, D. Howe, G.W. Jewell, Analysis and design optimization of an improved axially magnetized tubular permanent-magnet machine, IEEE Trans. Energy Convers. 19 (2) (2004) 289–295, https://doi.org/10.1109/TEC.2004.827026. Jun.
[28] P.H. Hogan, J.D. Van de Ven, Dynamic modeling of a linear electromagnetic piston pump, presented at the, in: ASME/BATH 2017 Symposium on Fluid Power and Motion Control, American Society of Mechanical Engineers Digital Collection, 2017, https://doi.org/10.1115/FPMC2017-4324. Dec..
[29] I. Boldea, L.N. Tutelea, W. Xu, M. Pucci, Linear electric machines, drives, and MAGLEVs: an overview, IEEE Trans. Ind. Electron. 65 (9) (2018) 7504–7515, https://doi.org/10.1109/TIE.2017.2733492. Sep.
[30] M. Petkovšek, M. Hočevar, M. Dular, Visualization and measurements of shock waves in cavitating flow, Exp. Therm. Fluid Sci. 119 (2020) 110215, https://doi.org/10.1016/j.expthermflusci.2020.110215. Nov.
[31] H. Shamsborhan, O. Coutier-Delgosha, G. Caignaert, F. Abdel Nour, Experimental determination of the speed of sound in cavitating flows, Exp. Fluids 49 (6) (2010) 1359–1373, https://doi.org/10.1007/s00348-010-0880-6. Dec.